Experimental and numerical investigation of a novel all-steel assembled core-perforated buckling-restrained brace

Zhou Yun [a,*], Yongsheng Cao [a], Jiro Takagi [b], Genquan Zhong [c], Zhiming He [a]

[a] *School of Civil Engineering, Guangzhou University, Guangzhou, Guangdong 510006, China*
[b] *Graduate School of Urban Env. Sciences, Tokyo Metropolitan Univ., 1-1 Minami-osawa Hachioji Tokyo, 192-0397, Japan*
[c] *School of Civil and Transportation Engineering, Guangdong University of Technology, Guangzhou, Guangdong 510006, China*

A B S T R A C T

A novel all-steel assembled buckling-restrained brace with a perforated plate core (PSBRB) is proposed. The seismic performance of the PSBRB is evaluated and compared with that of traditional all-steel assembled buckling-restrained braces with an imperforate plate core (SBRB). Two groups of PSBRBs and SBRBs with the same design parameters are tested and numerically simulated, focusing on their mechanical properties, fatigue properties, energy dissipation capacity, stress distribution, and high-order deformation patterns. The results are summarized as follows: 1) SBRBs and PSBRBs have similar mechanical properties; however, the novel PSBRB exhibits better ductility, fatigue properties, and cumulative energy dissipation capacity; 2) A high-stress concentration develops at the junction of the stopper and yield segment of the SBRB, but this problem can be solved by perforating the core and using the new bolt anti-skid method of the PSBRB; 3) The high-order deformation patterns of the PSBRB are different from those of the SBRB under compression; 4) It is recommended that the design restraining ratio of the PSBRB should be greater than 1.5.

1. Introduction

Braces can effectively increase the lateral stiffness of frame structures, as they are one of the main lateral force-resisting members. However, braces are prone to buckling under compression during earthquakes, resulting in a decrease in their load-carrying capacity. Buckling-restrained braces (BRBs) have been proposed to maintain the load-carrying capacity of braces under compression. Since their invention in the late 1980s [1–3], BRBs have been thoroughly studied and widely adopted globally. BRBs commonly comprise a core, restraining components, and unbonding materials. The core is the main energy dissipation component and typically consists of low-yield steel. The restraining components, commonly comprising concrete or metal, limit core buckling under compression, while unbonding materials reduce the friction between the core and restraining components [4–8]. BRBs have several advantages, including a buckling-restrained load-carrying capacity that does not decrease under compression and yielding capabilities to dissipate seismic energy to protect structural members from earthquake damage [4–8].

Concrete-filled steel tube BRBs are currently the most popular and mature configuration. However, they have several disadvantages,

including their heavy weight, large size, and complicated curing process for materials such as concrete or mortar [4–8]. Therefore, researchers and practitioners have proposed different types of BRBs to overcome these disadvantages. All-steel BRBs have the advantages of being lightweight, highly compact, and easy to process. They are made of steel plates or tubes and are only assembled by bolts or welding. To date, various all-steel BRBs have been proposed. Kato et al. [9] proposed a double steel tube BRB, composed of an inner-core steel tube and an outer restraining steel tube, and performed an analytical study. They found a problem with the double steel tube BRB, where the inner-core steel tube is prone to inward depression buckling under compression. Haganoya et al. [10] and Takeita et al. [11] solved this problem by installing an inner restraining steel tube inside the inner-core steel tube made of a triple steel tube BRB. They conducted a series of tests and numerical simulations to investigate the mechanical properties and energy dissipation capacity of the triple steel tube BRB. Due to the limitations of steel tube specifications, the design of BRBs cannot be adapted to meet specific load-carrying capacity requirements. Therefore, scholars have proposed all-steel BRBs, with lattice section or in-line section cores. Narihara et al. [12] and Koetaka et al. [13] proposed a steel tube restrained lattice section all-steel BRB, with a core restrained by four square steel tubes at each side of the core web. Fukuda et al. [14]

Abbreviations

BRB	buckling-restrained brace
SBRB	steel plate assembled buckling-restrained brace
PSBRB	core-perforated steel plate assembled buckling-restrained brace
FEA	finite element analysis
CPD	cumulative plastic deformation

Symbols

L	total length of the specimens
L_y	total length of the yield segments
A_y	cross-section area of the yield segment
L_c	total length of the connection segments
A_c	cross-section area of the connection segments
L_t	total length of the transition segments of SBRB
A_t	equivalent cross-section area of the transition segments of SBRB
L_{t1}	total length of the core transition segments of PSBRB
L_{t2}	total length of the core connection transition segments of PSBRB
A_{t1}	cross-section area of the core transition segment of PSBRB
A_{t2}	equivalent cross-section area of the connection transition segment of PSBRB
L_s	length of the stopper of SBRB
A_s	cross-section area of the stopper of SBRB
t	thickness of the core
E	Young's modulus
f_y	yield stress of steel
E'	post-yield Young's modulus
f_u	ultimate strength of steel
δ	elongation of steel
F_y	yield force
K	initial stiffness
d	yield displacement

t	thickness of the core
K_{PSBRB}	stiffness of PSBRB
K_{SBRB}	stiffness of SBRB
K_c	total stiffness provide by two connection segments
K_t	total stiffness provide by two transition segments
K_y	total stiffness provide by the yield segment
K_{t1}	total stiffness provide by two connection segments of PSBRB
K_{t2}	total stiffness provide by two connection transition segments of PSBRB
ξ	restraining ratio
P_E	overall elastic buckling load
I_r	moment of inertia of restrained components
α	post-yield stiffness ratio
β	compression strength adjustment factor
ζ	equivalent viscous damping ratio
Δ_{ci}	maximum compression deformation at the i-th loading cycle
Δ_{ti}	maximum tensile deformation at the i-th loading cycle
ε	strain
σ_0	yield stress at zero plastic strain
Q_∞	maximum change value of yield surface
b	change range of yield surface size with the development of plastic strain
C_1	1st initial follow-up strengthening modulus
C_2	2nd initial follow-up strengthening modulus
C_3	3rd initial follow-up strengthening modulus
γ_1	1st reduction rate of the follow-up strengthening modulus with plastic deformation
γ_2	2nd reduction rate of the follow-up strengthening modulus with plastic deformation
γ_3	3rd reduction rate of the follow-up strengthening modulus with plastic deformation

proposed an angle steel restrained lattice section all-steel BRB, with a core restrained by four angle steels connected by high-strength bolts. Zhou et al. [15,16] proposed an all-steel plate assembled BRB with an in-line section core to simplify the manufacturing of BRBs. The cores, stiffeners, restraining steel plates, and filling plates of their BRB were made of steel plates cut by a laser. All the parts were assembled using high-strength bolts, except for the welding between the core plate and the stiffeners, thus significantly reducing the manufacturing time. As a metallic damper, BRBs dissipate seismic energy mainly through plastic deformation, and early plasticity improves their energy dissipation capacity. The core-perforated BRBs exhibit this characteristic. The yield force is reduced by opening the holes in the core, inducing plasticity and dissipating seismic energy. Many researchers have proposed core-perforated BRBs. Zhou et al. [17] and Deng et al. [18] proposed and investigated the application of a triple steel tube perforated BRB using a core steel tube with slit holes. Cahís et al. [19] and Piedrafita et al. [20] proposed an all-steel plate perforated BRB and carried out further experimental research. Although these core-perforated BRBs show excellent performance, mass production is a challenge due to the high cost and complex processing.

In this study, a novel all-steel assembled buckling-restrained brace with a perforated plate core (PSBRB) is proposed. It combines the advantages of all-steel plate assembled BRBs and core-perforated BRBs, such as a small volume, lightweightedness, ease of fabrication, and ease of yield under earthquake conditions. The components of the proposed PSBRB consist only of steel plates cut by a laser and assembled by bolts. A traditional BRB usually needs to cure concrete or mortar for

approximately one month. However, the proposed PSBRB does not require this process and can be used immediately, significantly reducing the time costs. Furthermore, the proposed PSBRB is sufficiently thin to hide inside the wall. The seismic performance of this novel PSBRB is studied and compared with that of a traditional all-steel assembled plate buckling-restrained brace with an imperforate plate core (SBRB) [15]. Two groups of PSBRBs and SBRBs with the same design parameters (stiffness, yield strength, yield displacement, and core yield length) are tested and numerically simulated to analyze their mechanical properties, fatigue properties, energy dissipation capacity, stress distribution, and high-order deformation patterns.

2. Specimen composition and design

2.1. Specimen description

The composition of the proposed PSBRB and SBRB are shown in Fig. 1(a) and Fig. 1(b), respectively. Both the PSBRB and SBRB were designed to include the following main components: (1) steel core; (2) two restraining plates; (3) unbonding material; (4) two filling plates; (5) high-strength bolts. The steel core was the main energy dissipation component. Two restraining plates and two filling plates formed the restraining component, preventing the core from buckling under compression. There was a gap of 1 mm between the core and restraining component to avoid excessive global buckling under compression, and the rubber, as an unbonding material, was filled for lubrication. High-strength bolts were used to connect the restraining and filling plates.

I. Overall configuration of PSBRB

II. Assembly of PSBRB

III. Configuration of the core

(a) PSBRB

I. Overall configuration of SBRB

II. Assembly of SBRB

III. C onfiguration of the core

(b) SBRB

Fig. 1. Configuration of PSBRB and SBRB.
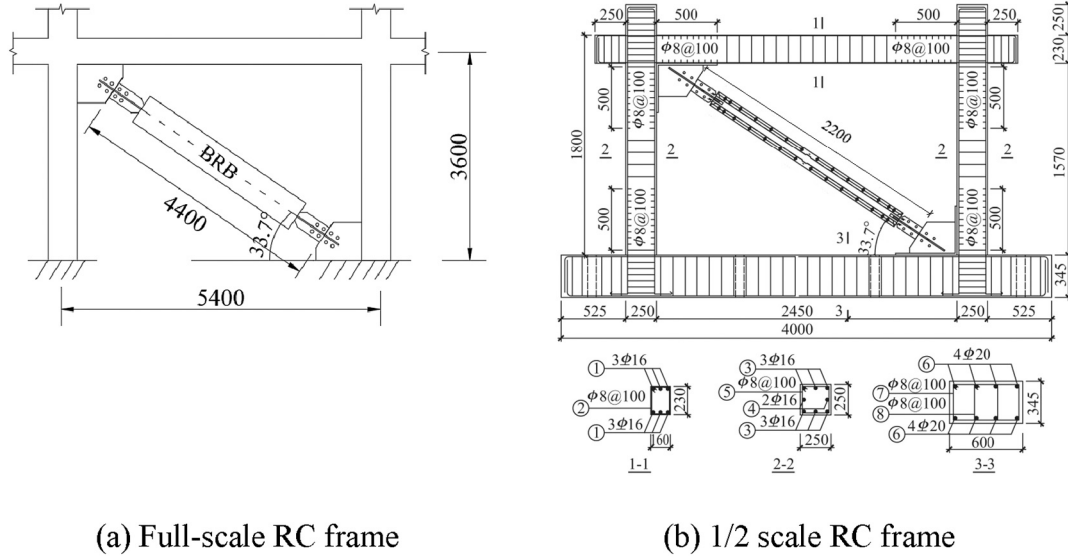
(a) Full-scale RC frame

(b) 1/2 scale RC frame

Fig. 2. Designed BRB for RC frame [21].

The difference between the PSBRB and SBRB was the perforation of the core. SBRB limited the restraining component to sliding by a stopper, which is a short segment with a cross-sectional area slightly larger than that of the middle yield segment. PSBRB limited the restraining component to sliding by central bolts (bolt anti-skid method).

The assembly process of the specimens was as follows: 1) all-steel components were cut using a laser; 2) stiffeners were welded on the core plate; 3) rubber was pasted onto the core; 4) all components were assembled using high-strength bolts.

2.2. Theoretical derivation

(1) Initial stiffness:

The initial stiffness of the PSBRB (K_{PSBRB}) can be calculated using Eq. (1) as follows:

$$K_{PSBRB} = \frac{1}{\frac{1}{K_c} + \frac{1}{K_{t2}} + \frac{1}{K_{t1}} + \frac{1}{K_y}} \tag{1}$$

where K_c, K_{t2}, K_{t1}, and K_y are the total stiffness provided by the two connection segments, two connection transition segments, all core transition segments, and all yield segments, respectively. These parameters can be calculated using Eq. (2) as follows:

$$K_c = \frac{E \cdot A_c}{L_c}; K_{t2} = \frac{E \cdot A_{t2}}{L_{t2}}; K_{t1} = \frac{E \cdot A_{t1}}{L_{t1}}; K_y = \frac{E \cdot A_y}{L_y} \tag{2}$$

where E is Young's modulus; A_c, A_{t2}, A_{t1}, and A_y are the cross-sectional area of the connection segments, equivalent cross-sectional area of the connection transition segments, cross-sectional area of the core transition segments, and cross-sectional area of the yield segments, respectively; L_c, L_{t2}, L_{t1}, and L_y are the total lengths of the connection segments, connection transition segments, core transition segments, and yield segments, respectively. Because the length of the curved segments in openings is small, and the variation of the cross-section of the curved segments is also small, the variation of the cross-section of the curved segments has little effect on the initial stiffness of the PSBRB; therefore, for ease of calculation, the cross-sectional area of the curved segments is assumed to be the same as that of the yield segments. And as the cross-sectional area of the connection transition segments (A_{t2}) varies linearly, it can be equivalently calculated according to Eq. (3):

$$A_{t2} = \frac{A_c - A_{t1}}{lnA_c - lnA_{t1}} \tag{3}$$

The initial stiffness of the SBRB (K_{SBRB}) can be calculated using Eq. (4) as follows:

$$K_{SBRB} = \frac{1}{\frac{1}{K_c} + \frac{1}{K_t} + \frac{1}{K_y} + \frac{1}{K_s}} \tag{4}$$

where K_c, K_t, K_y, and K_s are the total stiffness provided by two connection segments, two transition segments, the whole yield segment, and the stopper, respectively. They can be calculated using Eq. (5) as follows:

$$K_c = \frac{E \cdot A_c}{L_c}; K_t = \frac{E \cdot A_t}{L_t}; K_y = \frac{E \cdot A_y}{L_y}; K_s = \frac{E \cdot A_s}{L_s} \tag{5}$$

where A_c, A_t, A_y, and A_s are the cross-sectional areas of the connection segments, equivalent cross-sectional area of the transition segments, cross-sectional area of the yield segment, and cross-sectional area of the stopper, respectively. L_c, L_t, L_y, and L_s are the total lengths of the connection segments, transition segments, yield segment, and stopper, respectively. The equivalent cross-sectional area of the transition segments (A_t) can be calculated according to Eq. (6):

$$A_t = \frac{A_c - A_y}{lnA_c - lnA_y} \tag{6}$$

(2) Yield force:

The yield force (F_y) of both the PSBRB and SBRB can be calculated using Eq. (7) as follows:

$$F_y = A_y \cdot f_y \tag{7}$$

where f_y is the yield stress of the steel.

(3) Yield displacement:

The yield displacement (d) of both the PSBRB and SBRB can be calculated using Eq. (8) as follows:

$$d = \frac{F_y}{K} \tag{8}$$

where K is the initial stiffness of the BRBs.

(4) Restraining ratio:

The restraining ratio (ξ) can be calculated using Eq. (9) [1] as follows:

$$\xi = \frac{P_E}{F_y} \tag{9}$$

where P_E is the overall elastic buckling load of the BRBs, which can be
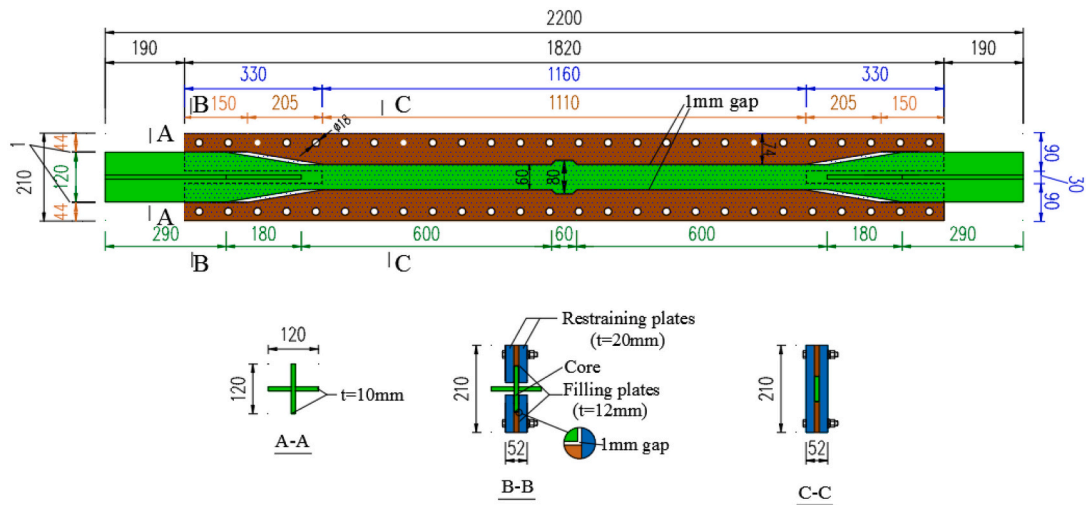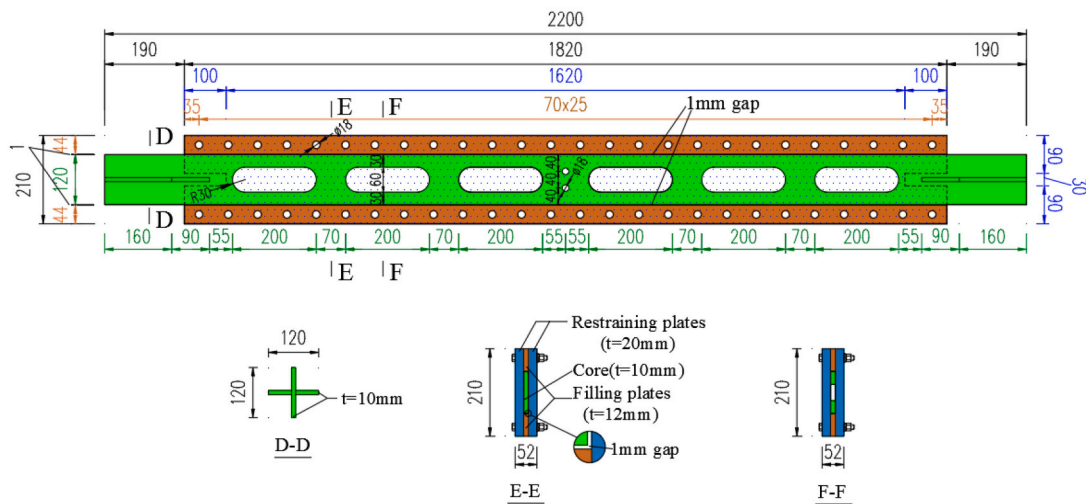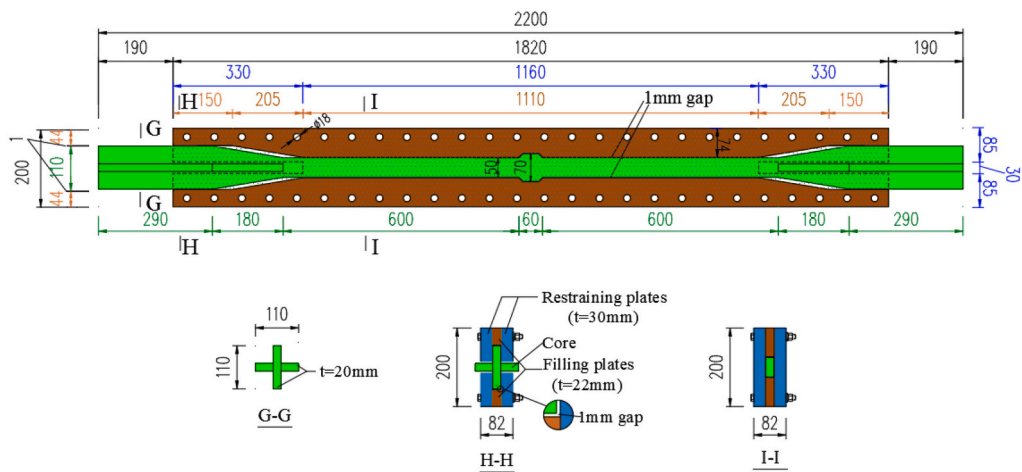
Fig. 3. Configurations of assembly components.
(All units in mm, t represents the thickness of the component)
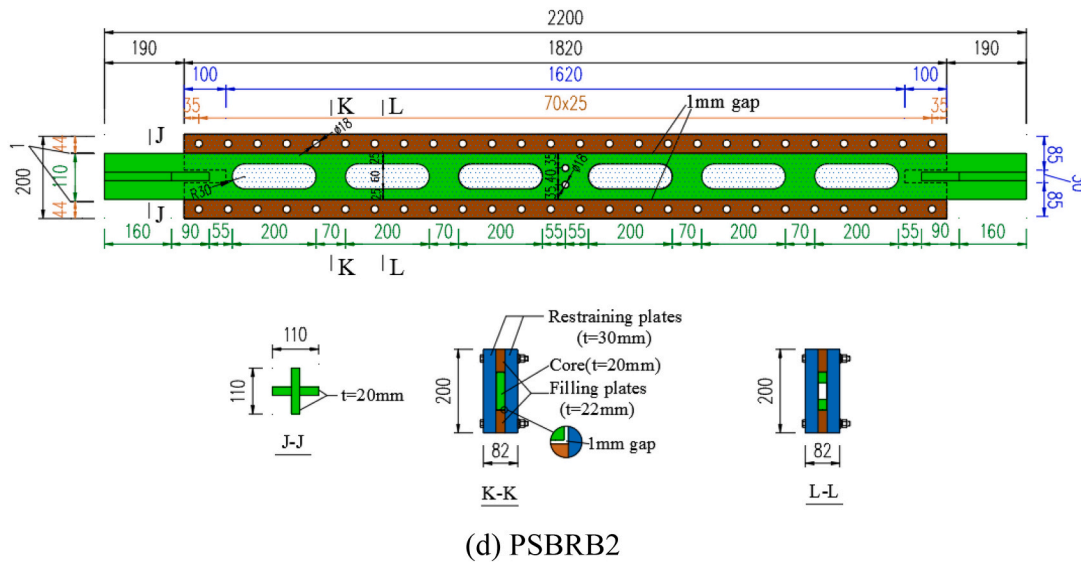
(d) PSBRB2

Fig. 3. (*continued*).

Table 1
Core dimensions.

Specimen	Yield segment			Transition segment		Connection segment		Stopper		Total length L (mm)
	L_y (mm)	t (mm)	A_y (mm²)	L_t (L_{t1}/L_{t2}) (mm)	A_t (A_{t1}/A_{t2}) (mm²)	L_c (mm)	A_c (mm²)	L_s (mm)	A_s (mm²)	
SBRB1		10	600	360	1265	580	2300	60	800	
PSBRB1	1200		600	500/180	1200/1691	320	2300	–	–	2200
SBRB2		20	1000	360	2164	580	4000	60	1400	
PSBRB2			1000	500/180	2200/3011	320	4000	–	–	

(t is the thickness of the core)

calculated using Eq. (10) as follows:

$$P_E = \frac{\pi^2 \cdot E \cdot I_r}{L^2} \tag{10}$$

where E is the Young's modulus, I_r is the moment of inertia of the restraining components, which is calculated based on the cross-section of the restraining components where the yield segment is, L is the total length of the BRB.

2.3. Specimen design

The specimens were designed for a 1/2 scale RC frame [21], as shown in Fig. 2. The stiffness of the designed frame was 40.43 kN/mm, and the required length of the BRB was 2200 mm. Two groups of SBRB and PSBRB specimens were designed with a stiffness ratio (the ratio of lateral stiffness provided by BRBs to the lateral stiffness provided by the frame) of 2:1 (BRB stiffness was approximately 80.9 kN/mm) and 3:1 (BRB stiffness was approximately 121.3 kN/mm), respectively. The SBRB and PSBRB with the same stiffness ratio had the same design parameters (stiffness, yield force, yield displacement, and total length of the yield segment). The SBRB and PSBRB with stiffness of 80.9 kN/mm were named as SBRB1 and PSBRB1, respectively; those with stiffness of 121.3 kN/mm were named as SBRB2 and PSBRB2, respectively.

The dimensions of all the components of the four specimens are shown in Fig. 3. Green, brown, and blue dimensions represent the core, restraining plates, and filling plates, respectively. The dimensions of each segment of the core for the four specimens are listed in Table 1. All components of the four specimens were made of mild steel Q235, widely employed in structural engineering in China. The material properties

Table 2
Material properties of steel.

Steel	E (GPa)	f_y (MPa)	E' (GPa)	f_u (MPa)	δ (%)
Q235	205	279.1	3.23	401	28

(E is the Young's modulus, f_y is the yield stress, E' is the post-yield Young's modulus, f_u is the ultimate strength, and δ is the elongation)

Table 3
Design mechanical properties.

Specimen	F_y (kN)	K (kN/mm)	d (mm)	Restraining ratio (ξ)
SBRB1		78.9	2.11	6.16
PSBRB1	167	77.3	2.16	6.14
SBRB2		132.5	2.11	**13.77**
PSBRB2	279	131.4	2.22	13.69

obtained from the coupon tests are presented in Table 2. Based on the coupon test results, the main design mechanical properties of the four specimens were calculated, as listed in Table 3. The restraining ratio (ξ) of all specimens was greater than 6.20, exceeding the recommended limit of greater than 1.5 in [1], indicating that the restraining component had sufficient restraint to the core.
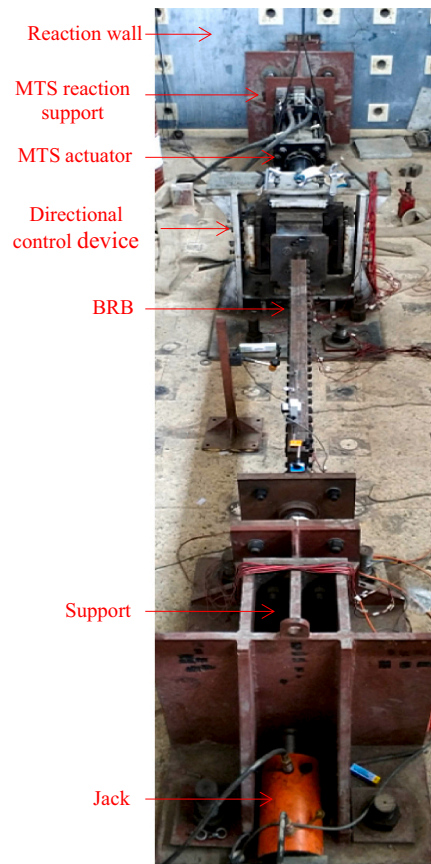
(a) Experimental setup.
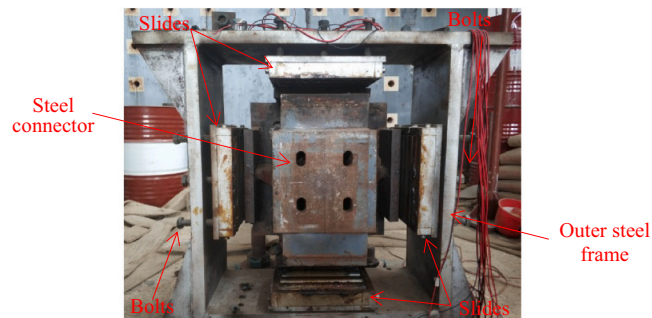
(b) Directional control device
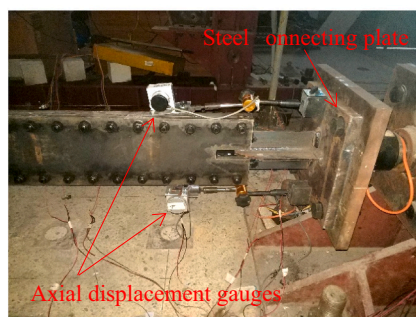
c) Axial displacement gauges

(d) Vertical displacement gauge

Fig. 4. Experimental setup and measuring devices.
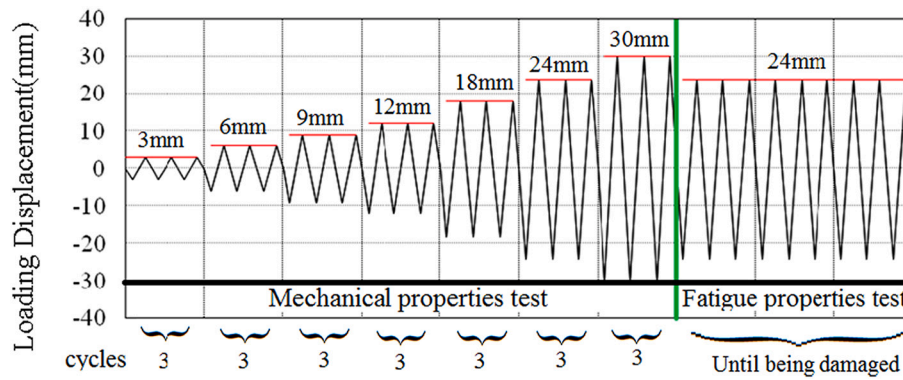
Fig. 5. Loading protocol.

3. Experimental program

3.1. Experimental setup and measuring devices

The experimental setup for the specimens is illustrated in Fig. 4(a), including a MTS actuator, directional control device, support, and jack.

The load and displacement capacities of the MTS actuator were $\pm$ 1000 kN and $\pm$ 50 mm, respectively. A directional control device, shown in Fig. 4(b), was used to prevent the loading end of the MTS actuator from straying during the test. It consisted of an outer steel frame, a steel connector used to connect the loading end of the MTS actuator to the specimens, and four slides at the four sides to reduce the friction between the steel connector and the outer steel frame. The bolts on the left and right sides of the outer steel frame could be screwed inward or outward to align the MTS actuator, steel connector, and specimen. There was a jack at the end of the support; a pressure of 30 MPa was applied to the support by the jack before the test to prevent the support from sliding.

The specimens were installed in the experimental setup after all components of the experimental setup were completely installed and debugged. In the installation process of the specimens, the steel connecting plates were welded to both ends of the specimens. The steel connecting plates were then connected to the experimental setup using high-strength bolts.

The measuring devices comprised two axial displacement gauges, a vertical displacement gauge, and several strain gauges. As shown in Fig. 4(c), two axial displacement gauges were installed at the top and bottom of the specimen to measure the axial net deformation of the specimens. As shown in Fig. 4(d), a vertical displacement gauge was installed at the middle of the specimen, to measure the global bending deformation of the specimens.

3.2. Loading protocol

The loading protocol was developed according to the *Specification for Seismic Tests of Buildings* (JGJ/T 101–2015) [22] in China. The four specimens were subjected to the same loading protocol, as shown in Fig. 5. Negative values are under compression and positive values are under tension. The experiments included tests of the mechanical and fatigue properties. In the mechanical properties test, the specimens were subjected to incremental cyclic displacements with amplitudes of 3, 6, 9, 12, 18, 24, and 30 mm to obtain their mechanical properties, and each amplitude was repeated three times. After the mechanical property test was completed, the specimens were subjected to cyclic displacements with an amplitude of 24 mm until they were damaged, to obtain their fatigue properties. The loading rate during the entire test process was 1 mm/s.

Table 4
Actual loading cycles.

	Loading amplitudes (mm)	SBRB1	PSBRB1	SBRB2	PSBRB2
	3	3	3	3	3
	6	3	3	3	3
	9	3	3	3	3
Mechanical properties test	12	3	3	3	3
	18	3	3	3	3
	24	3	3	3	3
	30	3	3	Damaged at 1st cycle	3
Fatigue properties test	24	Damaged at 5th cycle	Damaged at 26th cycle	–	Damaged at 1st cycle

4. Experimental results

4.1. Failure modes

No global buckling or local buckling was observed during the tests of the four specimens. The actual loading cycles at each loading amplitude for the four specimens are listed in Table 4. All specimens were damaged under tension. Specimen SBRB2 was damaged during the 1st loading cycle under a displacement of 30 mm in the mechanical property test. Specimens SBRB1, PSBRB1, and PSBRB2 completed all the mechanical property tests and were damaged at the 5th, 26th, and 1st loading cycles in the fatigue properties test, respectively.

After the test, the restraining components were removed to observe the failure modes of the core. The failure modes of the four specimens are illustrated in Fig. 6. The failure of both SBRB specimens was located at the junction of the stopper and yield segment; the failure of both PSBRB specimens was located at the perforated yield segment at one of the holes.

4.2. High-order deformation characteristics

As all specimens were damaged in tension, high-order deformation characteristics could not be realized by observing the core. However, when the specimens were under compression, unbonding materials were extruded because of the high-order deformation generated by the core. Therefore, the wavenumber of the high-order deformation generated by the core can be inferred by observing the extrusion shape of rubber on the restraining plate. The rubber shapes on the restraining plates of the four specimens are shown in Fig. 7. For ease of interpretation, a schematic diagram of the observation is presented. The shaded parts in the figure indicate where the rubber was extruded. By observing the number of crests and troughs generated in the rubber, the maximum
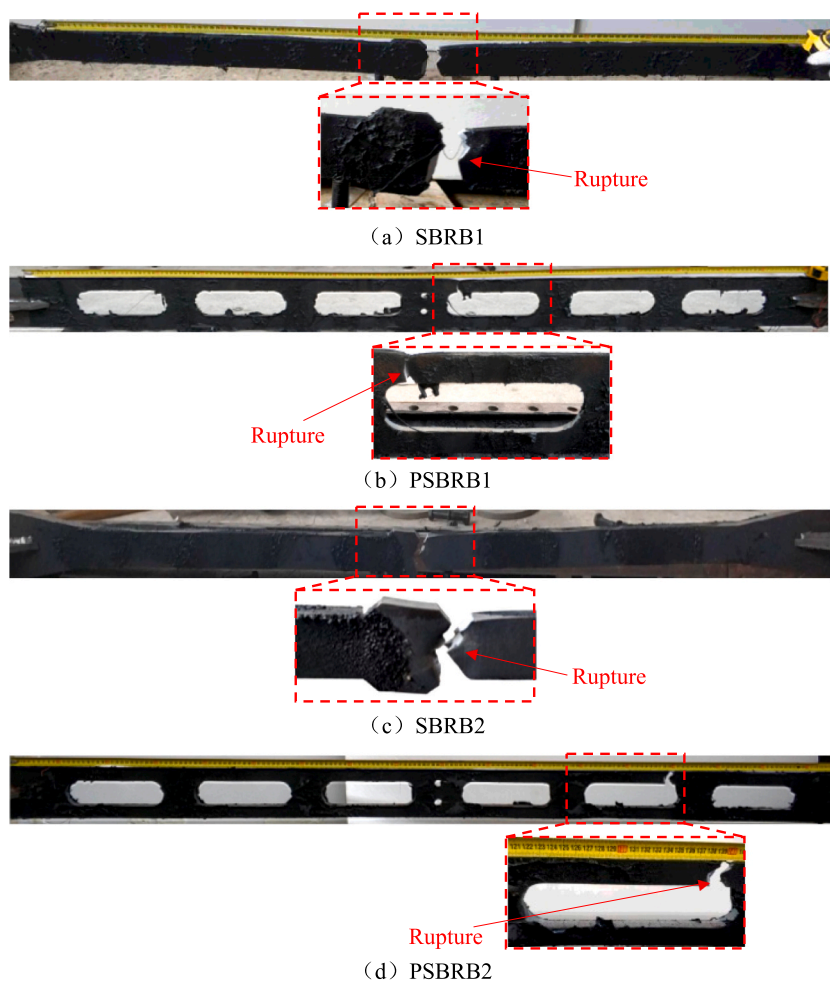
（a）SBRB1

（b）PSBRB1

（c）SBRB2

（d）PSBRB2

Fig. 6. Failure modes.

wavenumber of high-order deformation generated by the core can be inferred. As seen from Fig. 7, for specimen SBRB1, there were a total of 23 crests and troughs on the rubber, and the core could generate 12 orders of deformation. For specimen SBRB2, there was a total of 10 crests and troughs on the rubber, and the core could generate five orders of deformation. For specimen PSBRB1, there were three crests and troughs on the rubber on each yield segment at each hole, and each yield segment could generate three orders of deformation. For specimen PSBRB2, there were two crests and troughs on the rubber on each yield segment at each hole, and each yield segment could generate two orders of deformation. The above results show that the high-order deformation patterns of PSBRBs under compression are different from those of SBRBs. The wavenumber of the high-order deformation of SBRB1 and PSBRB1 with thinner cores was significantly greater than that of SBRB2 and PSBRB2 with thicker cores.

4.3. Hysteretic loops

The hysteretic loops of the axial force read by the MTS actuator compared to the axial deformation read by the axial displacement gauges of the four specimens are shown in Fig. 8. The backbone curves of the four specimens were obtained by connecting the maximum axial force at each loading amplitude in the hysteretic loops, as shown in Fig. 9. The mechanical properties of the four specimens were obtained based on the hysteretic loops and backbone curves listed in Table 5.

As shown in Fig. 8, the hysteretic loops of the four specimens were stable, plump, and symmetrical. Specimens SBRB1, PSBRB1, and PSBRB2 completed all the mechanical property tests with a maximum

displacement of 30 mm. However, specimen SBRB2 only completed three loading cycles under a displacement of 24 mm and was damaged at the 1st loading cycle under a displacement of 30 mm in the mechanical properties test. PSBRB2 showed better ductility than SBRB2, indicating that PSBRB had better ductility than SBRB with the same design parameters. Specimens SBRB1, PSBRB1, and PSBRB2 completed all the mechanical property tests and were damaged at the 5th, 26th, and 1st loading cycles in the fatigue properties test, respectively. PSBRB1 can be loaded for 21 more cycles than SBRB1 in the fatigue property test, exhibiting much better fatigue properties than SBRB1, indicating that PSBRB has better fatigue properties than SBRB with the same design parameters.

As shown in the backbone curves in Fig. 9, the axial force of the four specimens increased as the loading amplitude increased. The backbone curves of the four specimens exhibited a clear bilinear relationship. The shape of the backbone curve of specimen SBRB1 was similar to that of PSBRB1, and the axial force at the same loading amplitude was similar as the maximum difference was smaller than 10%; similar characteristics were observed for specimens of SBRB2 and PSBRB2. From Table 5, the differences in the actual mechanical properties (initial stiffness, yield force, and yield displacement) between specimens SBRB1 and PSBRB1 were within 10%; similar characteristics were observed for specimens of SBRB2 and PSBRB2. The above results show that SBRBs and PSBRBs with the same design parameters have similar mechanical properties.

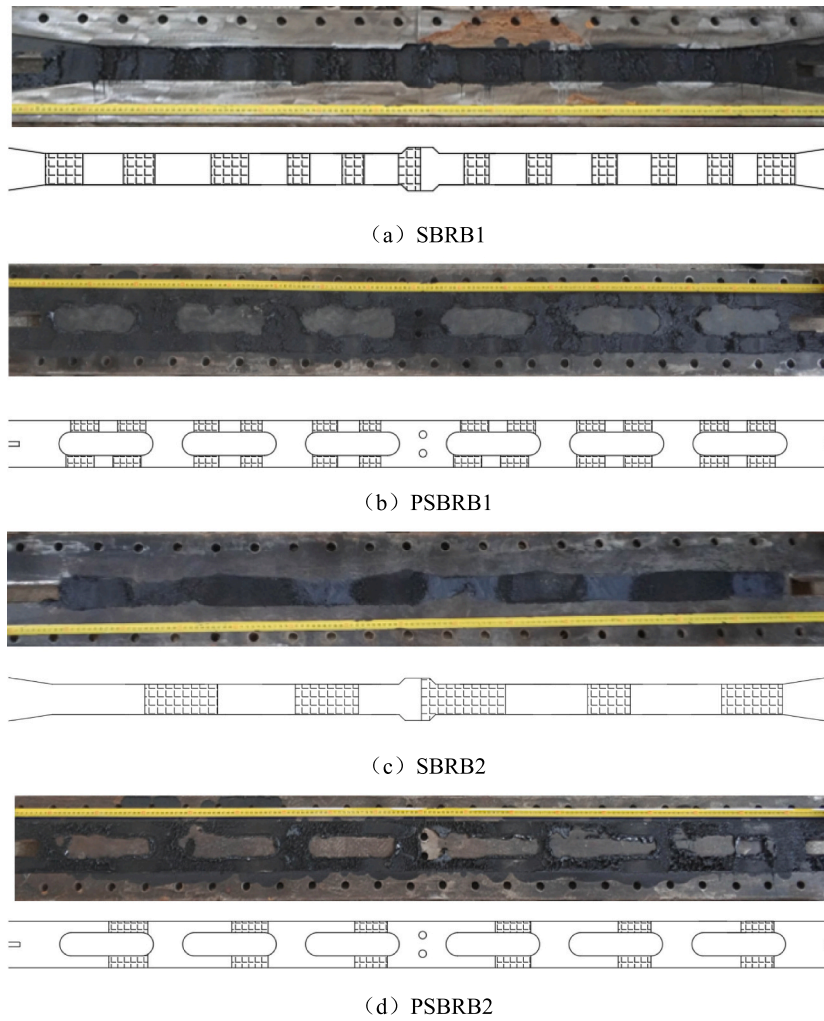The compression strength adjustment factor (β) can be calculated using Eq. (11) as follows:

（a）SBRB1

（b）PSBRB1

（c）SBRB2

（d）PSBRB2

Fig. 7. Extrusion shape of the rubber.
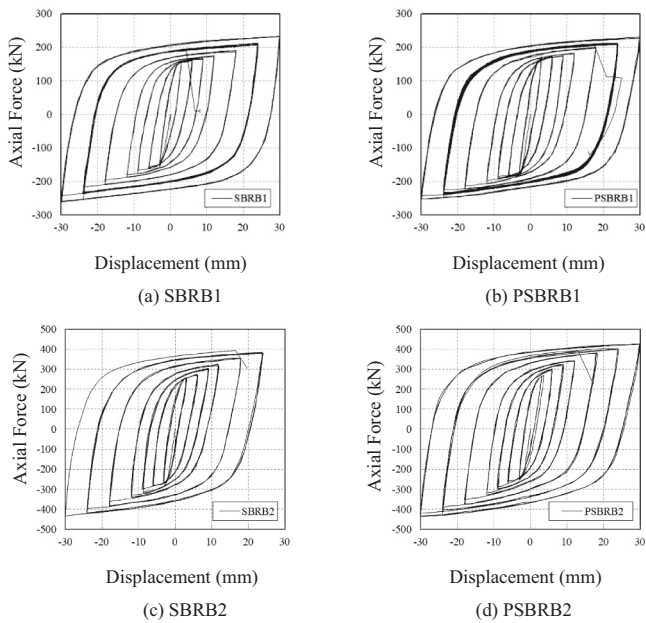

(a) SBRB1

(b) PSBRB1

(c) SBRB2

(d) PSBRB2

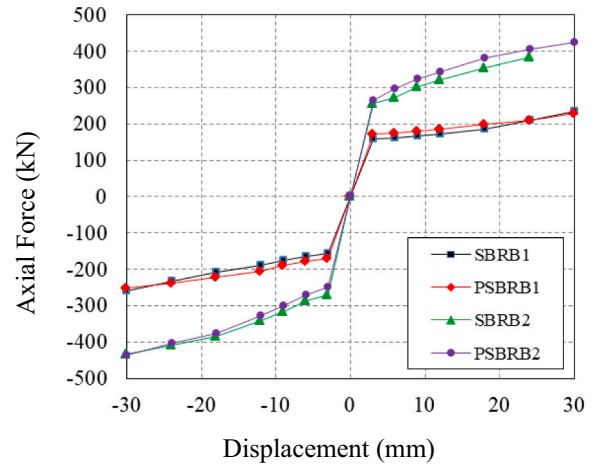**Fig. 8.** Hysteric loops.

Fig. 9. Backbone curve.

Table 5
Mechanical properties of the four specimens.

Specimen	K (kN/mm)	F_y (kN)	d (mm)	α (%)	β
SBRB1	75.8	159.6	2.11	3.70	1.11
PSBRB1	76.1	165.1	2.17	3.58	1.10
Difference	0.39%	3.44%	3.33%	3.35%	0.91%
SBRB2	128.1	275.2	2.14	4.44	1.06
PSBRB2	129.2	280.3	2.17	4.28	1.02
Difference	0.85%	1.82%	1.38%	3.74%	3.92%

(F_y denotes the yield force, K is the initial stiffness, d is the yield displacement, α is the post-yield stiffness ratio, β is the compression strength adjustment factor)
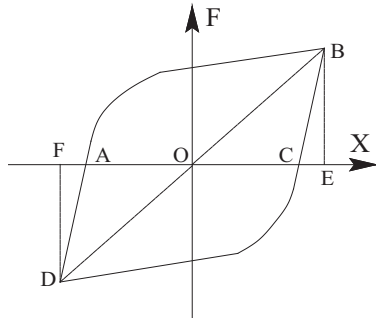
Fig. 10. Illustration of calculation method for equivalent viscous damping ratio.
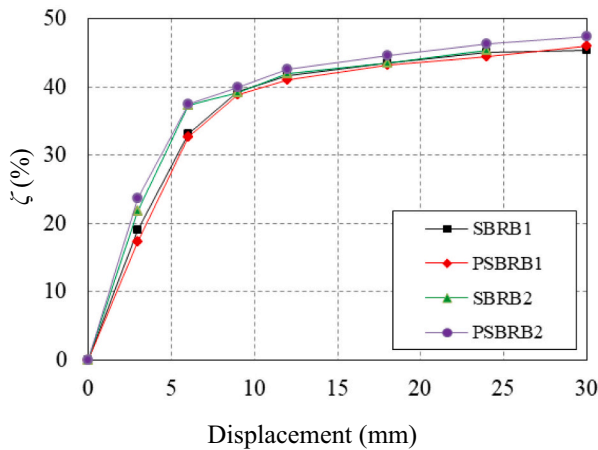
Fig. 11. Equivalent viscous damping ratio.

$$\beta = \frac{C_{max}}{T_{max}} \qquad (11)$$

where C_{max} is the maximum compression under maximum loading amplitude; T_{max} is the maximum tension under maximum loading amplitude.

From Table 5, the maximum β of the four specimens was 1.11. The β values of all specimens are in line with the design code [23], which specifies values of less than 1.30, indicating that both the SBRB and PSBRB have good mechanical symmetry.

4.4. Equivalent viscous damping ratio

The equivalent viscous damping ratio (ζ) is an important parameter for evaluating the energy dissipation capacity of BRBs. The larger ζ is, the better the energy dissipation capacity of the BRBs. ζ can be calculated using Eq. (12) as follows [24]:

Table 6
Cumulative plastic deformation.

Specimen	CPD
SBRB1	723
PSBRB1	1584
SBRB2	332
PSBRB2	585

$$\zeta = \frac{1}{2\pi} \cdot \frac{S_{ABC} + S_{CDA}}{S_{OBE} + S_{ODF}} \qquad (12)$$

where S_{ABC}, S_{CDA}, S_{OBE}, and S_{ODF} are illustrated in Fig. 10.

The ζ values of the four specimens at each loading amplitude are shown in Fig. 11, where the values are the averages of the three loading cycles under each loading amplitude. From Fig. 11, the ζ values of the four specimens increased as the loading amplitude increased. The ζ values of specimens SBRB1 and PSBRB1 were similar at the same loading amplitude, while the ζ value of specimen PSBRB2 was slightly larger than that of SBRB2 at a larger loading amplitude; however, the difference at each loading amplitude was within 5%. The above results indicate that the SBRB and PSBRB with the same design parameters have similar energy dissipation capacities.

4.5. Cumulative energy dissipation capacity

The cumulative energy dissipation capacity of BRBs can be evaluated by the cumulative plastic deformation (CPD) coefficient, calculated using Eq. (13) [22]:

$$CPD = \sum_{i=1}^{n} \left[\frac{2(|\Delta_{ci}| + |\Delta_{ti}|)}{d} - 4 \right] \qquad (13)$$

where n represents the total number of cyclic loadings, Δ_{ci} and Δ_{ti} are the maximum compressive and tensile deformations at the i-th loading cycle, respectively, and d is the yield displacement.

The CPD coefficients calculated for the four specimens are listed in Table 6. The CPD coefficient of PSBRB1 is 2.19 times that of SBRB1, and the CPD coefficient of PSBRB2 is 1.76 times that of SBRB2. The PSBRB showed a much better cumulative energy dissipation capacity than the SBRB with the same design parameters.

5. Numerical simulation

ABAQUS 6.14 [25] software was used to establish finite element models to analyze the stress distribution and high-order buckling characteristics of the specimens during the test.

5.1. Finite element modeling

The finite element models were established based on the size of the test specimens. As high-strength bolts have a strong connection ability to the restraining plates and filling plates, the restraining component can be simulated using both plates as they have no bolt holes and tie together. All components, including the core, restraining plates, filling plates, and bolts, were modelled using solid elements. The restraining plates and filling plates were very regular, therefore, C3D8I could be used as the elements of these components. To accurately reveal the stress distribution in the core, the element C3D20R, which is sensitive to stress concentration, was used as the elements of the core. C3D8R was used as the central bolt elements. The modeling and mesh of specimens PSBRB1 and SBRB1 are shown in Fig. 12. As the restraining plates and filling plates had sufficient strength that might not yield during analysis, the mesh size of these components was to a large size of 40 mm, and the mesh size of the core and bolts was approximately 10 mm. A local fine mesh was applied to the stopper and transition segments, which were
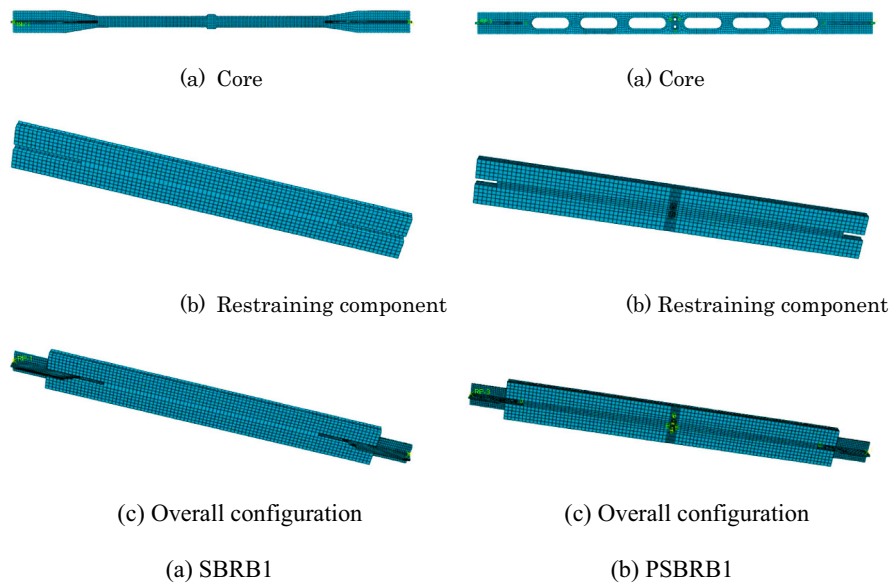
(a) Core

(a) Core

(b) Restraining component

(b) Restraining component

(c) Overall configuration

(c) Overall configuration

(a) SBRB1

(b) PSBRB1

Fig. 12. Modeling and mesh of the specimens SBRB1and PSBRB1.

Table 7
Constitutive model parameters of steel.

σ_0 (MPa)	Q_∞ (MPa)	b	C_1 (MPa)	γ_1	C_2 (MPa)	γ_2	C_3 (MPa)	γ_3
231.6	150	2.4	10,000	100	12,000	320	4000	1000

(σ_0 is the stress at 0 equivalent plastic strain; Q_∞ is the maximum change value of the yield surface; b is the change range of the yield surface size with the development of plastic strain; C_1, C_2, and C_3 are the 1st, 2nd, and 3rd initial follow-up strengthening modulus, respectively; γ_1, $\gamma_{2,}$ and γ_3 are the 1st, 2nd, and 3rd reduction rate of the follow-up strengthening modulus with plastic deformation, respectively).
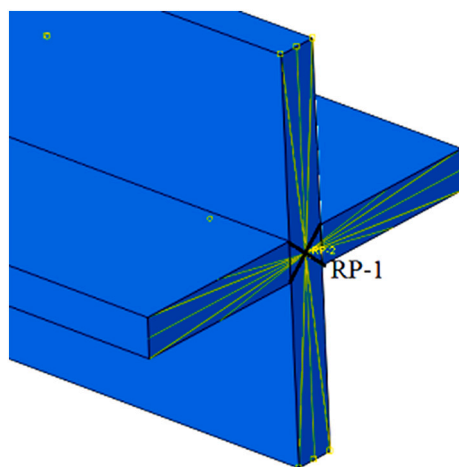
Fig. 13. End coupling.

prone to stress concentration. An initial bending imperfection of 2.2 mm (L/1000) was applied to the specimens before the analysis.

The constitutive model was based on the mixed hardening model [26], the parameters of which were obtained by fitting the material properties of Q235 steel, as shown in Table 2. The parameters are listed in Table 7.

Surface-to-surface contact was adopted between the core and the restraining component. Normal behavior was set as hard contact and

tangential behavior was set as a penalty. As the core was pasted with rubber for lubrication, the friction coefficient between the core and restraining component was set to 0.1, and the friction coefficient between the other components was set as 0.3. The same frictional coefficient was considered in similar analyses conducted by Chou & Chen [27] and Hoveidae & Rafezya [28]. The cross-sections at both ends of the core were coupled, as shown in Fig. 13. One side was fixed and the other side was loaded, similar to the experiments. The loading protocol was the same as in the experiments, but the fatigue properties were not tested.

5.2. Numerical results

5.2.1. Hysteretic loops
Fig. 14 shows a comparison of the hysteretic loops between the test and numerical simulation results. The hysteretic responses of the numerical simulations were approximately equal in the test results, and the analysis results can accurately and objectively reflect the real state of the specimens.

5.2.2. Stress distribution
The stress contours of the cores of the four specimens under a tensile displacement of 30 mm are shown in Fig. 15. The red circles in the figure represent the locations of the maximum stress, and the value next to the circle represents the maximum stress value.

As seen from Fig. 15, the maximum stresses of specimens SBRB1 and SBRB2 were located at the junction of the stopper and yield segment, and the maximum stresses of specimens PSBRB1 and PSBRB2 were located at the opening yield segment. The maximum stresses of the specimens SBRB1 and SBRB2 were 491.3Mpa and 489.2Mpa respectively, significantly larger than those of the specimens PSBRB1 and PSBRB2, 425.4Mpa and 424.7Mpa, respectively.

5.2.3. Equivalent plastic strain
The equivalent plastic strain (PEEQ) of the cores of the four specimens during the entire analysis process is shown in Fig. 16. The position of the high PEEQ of the SBRB was mainly located at the junction of the yield segment and stopper and at the peaks of high-order waves. The maximum PEEQs of specimens SBRB1 and SBRB2 were located at the junction of the yield segment; the values were 0.711 and 0.677, respectively. The PEEQ was evenly distributed at the opening yield segments of the PSBRB. The maximum PEEQ values of PSBRB1 and PSBRB2 were 0.618 and 0.611, respectively, significantly lower than
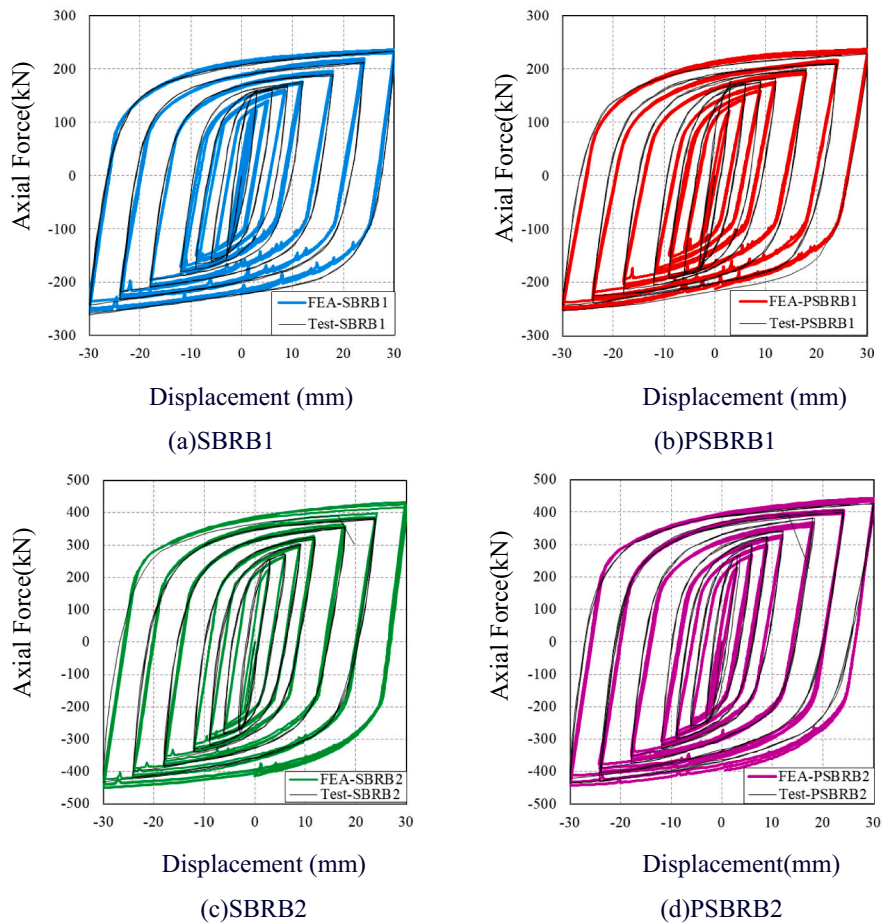
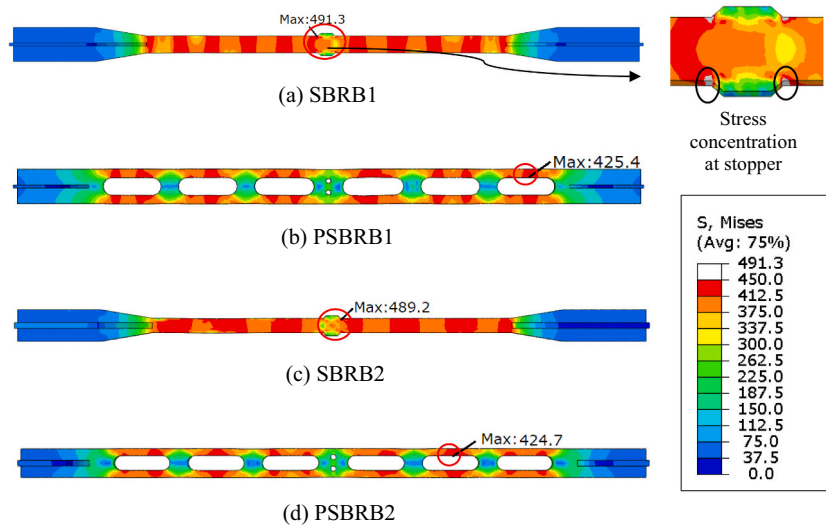**Fig. 14.** Comparison of test and FEA.

Fig. 15. Stress distributions.

those of SBRB1 and SBRB2.

Combined with the stress contour in Section 5.2.2, the maximum stress and PEEQ of the PSBRB were significantly lower than those of the SBRB with the same design parameters. This is because there was a section mutation at the junction of the stopper and the yield segment of the SBRB, prone to producing a high stress concentration; thus, there

was a high plastic strain. Once the cumulative plastic strain exceeded the fatigue limit of the steel, the brace fractured. Therefore, the ductility and fatigue properties of the yield segment of the SBRB could not be fully utilized because of the failure caused by the stress concentration at the junction of the stopper and the yield segment. However, this disadvantage can be addressed by perforating the core and applying the bolt anti-
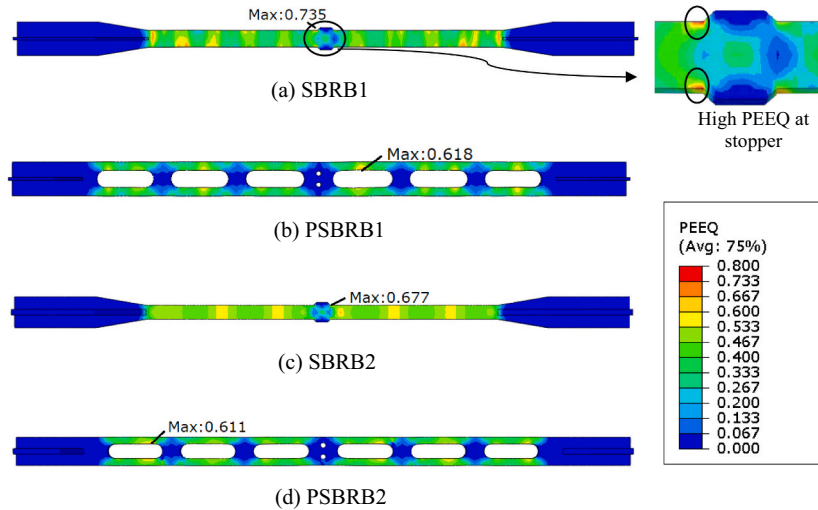
Fig. 16. Equivalent plastic strain.
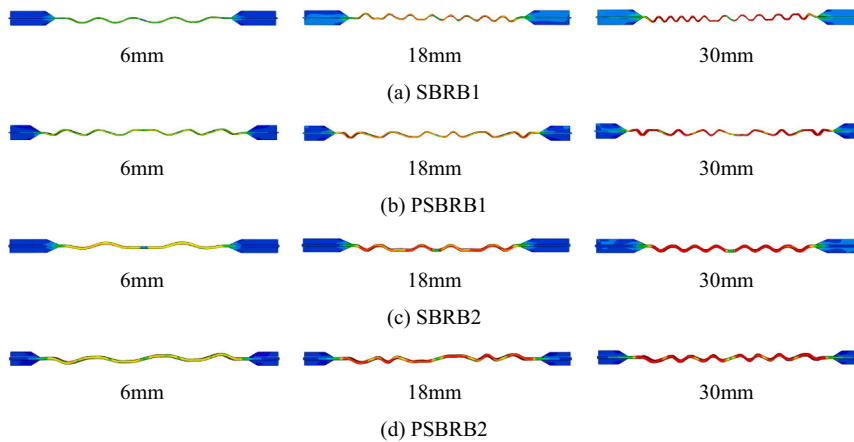
Fig. 17. High-order deformation under different compressive displacement.

skid method used in the PSBRB. Using smooth stopper bolt holes to replace the traditional stopper and opening holes in the core increased the load-carrying capacity of the core transition segment. Therefore, the stress concentration was reduced, with the maximum core stress located at the yield segment, implying that the ductility and fatigue properties of the yield segments of the PSBRB could be fully utilized. This is also the reason for the corresponding failure modes caused by the four specimens and the better ductility and cumulative energy dissipation performance of the PSBRB in the test. It should be noted that the design method of the core of the SBRB specimens in this study is used by some manufacturers; enlarging the radius of the edge of the stopper to reduce the rapid change in the cross-section might reduce the stress concentration and improve the ductility.

5.2.4. High-order deformation patterns

The high-order deformations of the four specimens under compressive displacements of 6, 18, and 30 mm are shown in Fig. 17. For ease of interpretation, the deformation in the weak axis of the BRB was magnified 20 times.

As seen from Fig. 17, the high-order deformation formation process of the SBRB was that 1st-order buckling was generated at the yield segment, and higher-order buckling was generated at the yield segment as the compressive displacement increased. In the PSBRB, 1st-order buckling was generated at each yield segment at each hole, and

Table 8
Relationship between restraining plate and restraining ratio

Specimens	t_r (mm)	restraining ratio (ξ)
PSBRB1-5 mm	5	0.42
PSBRB1-6 mm	6	0.56
PSBRB1–8 mm	8	0.92
PSBRB2-5 mm	5	0.67
PSBRB2–6 mm	6	0.83
PSBRB2-8 mm	8	1.22

higher-order buckling was generated at each yield segment as the compressive displacement increased. The wavenumbers of the higher-orders of specimens SBRB1 and PSBRB1 with thinner cores were significantly higher than those of specimens SBRB2 and PSBRB2 with thicker cores, under the same compressive displacement.

5.2.5. Impacts of restraining ratio

Fujimoto et al. [1] recommended that the restraining ratio of the imperforate dog-bone core BRBs should be greater than 1.5. PSBRB1 and PSBRB2 with different restraining ratios were analyzed to study the influence of different restraining ratios on the stability of PSBRB. The restraining ratio was changed by changing the thickness of the restraining plate (t_r), and the relationship is shown in Table 8.
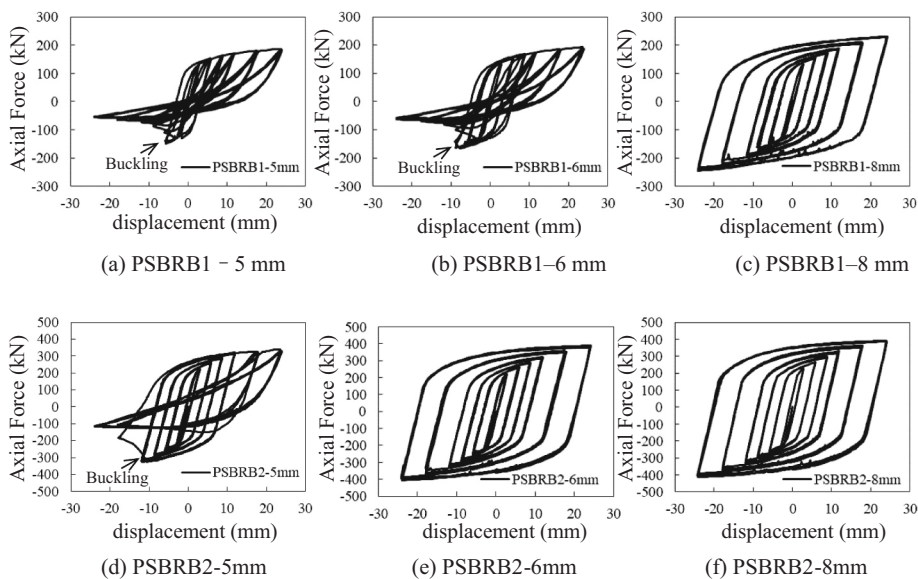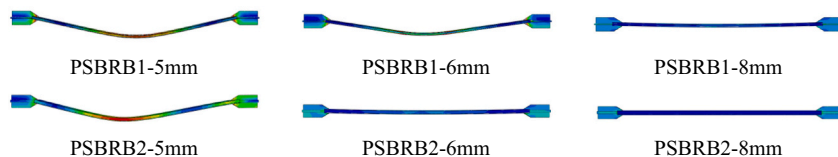
Fig. 18. Hysteric loops.

Fig. 19. Global deformation in weak axial.

The hysteretic loops of the PSBRB with different restraining ratios obtained by the analysis are shown in Fig. 18, and the global deformation of the BRB under the maximum displacement is shown in Fig. 19. As seen from Figs. 18 and 19, PSBRB1 and PSBRB2 did not buckle when the restraining ratio reached or exceeded 0.92 and 0.83, respectively. PSBRB1 and PSBRB2 buckled when the restraining ratios were less than 0.56 and 0.67, respectively, and the buckling mode was C-shaped. According to the above analysis results, buckling of the PSBRB can be avoided when the restraining ratio is larger than 1.0. However, considering the safety surplus, the restraining ratio of the PSBRB is recommended to exceed 1.5, which is consistent with the recommended value in Fujimoto et al. [1].

6. Conclusion

In this study, a novel all-steel assembled buckling-restrained brace with a perforated plate core (PSBRB) was proposed. Two groups of PSBRBs and traditional all-steel assembled plate buckling-restrained braces (SBRBs) with the same design parameters (equal stiffness, yield strength, yield displacement, and yield length of the core) were tested and numerically simulated to study their mechanical properties, energy dissipation capacity, stress distribution, and high-order deformation patterns. The following results were obtained:

(1) The proposed PSBRB exhibited good mechanical properties, stability, and energy dissipation capacity.

(2) The experimental results show that the difference in mechanical properties (yield stress, yield displacement, and initial stiffness) between the SBRB and PSBRB groups with the same design parameters was less than 5%, indicating that SBRB and PSBRB have similar mechanical properties. However, PSBRB showed much better ductility, fatigue properties, and cumulative energy dissipation capacity.

(3) A high-stress concentration was easily produced at the junction of

the stopper and the yield segment of the SBRB, resulting in a high PEEQ. Therefore, failure usually occurs at this location. However, this issue can be addressed by perforating the core and the bolt anti-skid method used in the PSBRB.

(4) The high-order deformation formation process of the SBRB was that 1st-order buckling was generated at the yield segment, and higher-order buckling was generated at the yield segment as the compressive displacement increased. In the PSBRB, 1st-order buckling was generated at each yield segment at each hole, and higher-order buckling was generated at each yield segment as the compressive displacement increased.

(5) In the finite element analysis, models PSBRB1–8 mm and PSBRB2–6 mm with a restraining ratio less than 1.0 did not buckle. Therefore, buckling could be avoided when the restraining ratio of the PSBRB exceeded 1.0. Considering the safety margin, the restraining ratio of the PSBRB is recommended to be greater than 1.5.

CRediT authorship contribution statement

Zhou Yun: Conceptualization, Methodology, Resources, Investigation, Writing – original draft, Supervision. **Yongsheng Cao:** Methodology, Investigation, Formal analysis, Data curation, Writing – original draft. **Jiro Takagi:** Methodology, Writing – review & editing. **Genquan Zhong:** Resources. **Zhiming He:** Writing – review & editing.

Declaration of Competing Interest

The authors declare that they have no known competing financial interests or personal relationships that could have appeared to influence the work reported in this paper.

Acknowledgements

References

[1] M. Fujimoto, A. Wada, E. Saeki, A. Watanabe, Y. Hitomi, A study on the unbonded brace encased in buckling-restraining concrete and steel tubes, J. Struct. Constr. Eng .(Trans. AIJ) 34B (1988) 249–258 (in Japanese).

[2] M. Fujimoto, A. Wada, E. Saeki, A. Watanabe, Y. Hitomi, A study on brace enclosed in buckling-restrained mortar and steel Tubes (Part 1). Annual Research Meeting Architectural Institute of Japan, Kanto, Japan, C-1, Structures II, 1988, pp. 1339–1340 (10). (in Japanese).

[3] M. Fujimoto, A. Wada, E. Saeki, A. Watanabe, Y. Hitomi, A study on brace enclosed in buckling-restrained mortar and steel tubes (Part 2). Annual Research Meeting Architectural Institute of Japan, Kanto, C-1, Structures II, 1988, pp. 1341–1342 (10). (in Japanese).

[4] T. Takeuchi, Buckling-Restrained Braces and Applications, JSSI Press, Tokyo, Japan, 2017.

[5] T. Takeuchi, Buckling-restrained brace: History, design and applications, Key Eng. Mater. 763 (2018) 50–60, https://doi.org/10.4028/www.scientific.net/KEM.763.50.

[6] Y. Zhou, H. Shao, Y. Cao, E.M. Lui, Application of buckling-restrained braces to earthquake-resistant design of buildings: a review, Eng. Struct. 246 (2021) 112991, https://doi.org/10.1016/j.engstruct.2021.112991.

[7] Y. Zhou, Design and Application of Buckling-Restrained Braced Frames, China Building Industry Press, Beijing, China, 2007 (in Chinese).

[8] M. Fujimoto, A. Wada, E. Saeki, T. Takeuchi, A. Watanabe, Development of unbonded brace, Quarterly Column 115 (1990) 91–96.

[9] M. Kato, A. Kasai, X. Ma, T. Usami, An analytical study on the cyclic behavior of double-tube type buckling-restrained braces, Struct. Eng. Trans. 50A (2004) 103–112 (in Japanese).

[10] M. Haganoya, T. Nagao, T. Taguchi, K. Takeita, Studies on buckling-restrained bracing using triple steel tubes: Part 1: outline of triple steel tube member and static cyclic loading tests. Annual Research Meeting Architectural Institute of Japan, Kinki, C-1, Structures III, 2005, pp. 1011–1012 (9). (in Japanese).

[11] K. Takeita, T. Nagao, T. Taguchi, M. Haganoya, Studies on buckling-restrained bracing using triple steel tubes: Part 2: Consideration on experimental results and FEM analyses. Annual Research Meeting Architectural Institute of Japan, Kinki, C-1, Structures III, 2005, pp. 1013–1014 (9). (in Japanese).

[12] H. Narihara, O. Tsujita, Y. Koetaka, The experiental study on buckling restrained braces: Part1: Experiment on pin connection type. Annual Research Meeting Architectural Institute of Japan, Tohoku, C-1, Structures III, 2000, pp. 911–912 (9). (in Japanese).

[13] Y. Koetaka, O. Tsujita, H. Narihara, The experiental study on buckling restrained braces: Part1: Experiment on fixed connection type. Annual Research Meeting Architectural Institute of Japan, Tohoku, C-1, Structures III, 2000, pp. 913–914 (9). (in Japanese).

[14] K. Fukuda, T. Makino, Y. Ichinohe, Development of Brace-type hysteretic dampers. Annual Research Meeting Architectural Institute of Japan, Hokkaido, C-1, Structures III, 2004, pp. 867–868 (8). (in Japanese).

[15] Y. Zhou, G. Zhong, Q. Chen, C. Gong, Experimental study on hysteretic performance of steel-plate assembled buckling-restrained braces with different constructional details, China Civil Eng. J. 50 (17) (2017) 9–17 (in Chinese).

[16] Y. Zhou, R. Yin, W. Zhang, H. Ji, X. Deng, S. Han, Experimental study on hysteretic performance of steel-plate assembled buckling-restrained brace, J. Build. Struct. 35 (8) (2014) 37–43 (in Chinese).

[17] Y. Zhou, X. Deng, H. Qian, H. Chu, An experimental study of the perforation-type triple-steel tube buckling-restrained brace, China Civ. Eng. J. 43 (09) (2010) 77–87 (in Chinese).

[18] X. Deng, H. Chu, H. Qian, Y. Zhou, L. Chen, The finite element modeling analysis of triple-steel tube buckling-restrained brace performance, J Huazhong Univ Sci Technol (Urban Sci Ed) 25 (03) (2008) 99–103 (in Chinese).

[19] X. Cahís, E. Simon, D. Piedrafita, A. Catalan, Core behavior and low-cycle fatigue estimation of the perforated core buckling-restrained brace, Eng. Struct. 174 (2018) 126–138, https://doi.org/10.1016/j.engstruct.2018.07.044.

[20] D. Piedrafita, X. Cahís, E. Simon, J. Comas, A new perforated core buckling-restrained brace, Eng. Struct. 85 (2015) 118–126.

[21] G. Zhong, Y. Zhou, Y. Cao, X. Deng, Q. Chen, Experimental study on out-of-plane mechanical performance of steel-plate assembled buckling-restrained braced RC frame, China Civ. Eng. J. 53 (11) (2020) 77–87 (in Chinese).

[22] JGJ/T101–2015, Specification for seismic test of buildings. Beijing, China: Ministry of Housing and Urban-Rural Development of the People's Republic of China, 2015 (in Chinese).

[23] JGJ297–2013, Technical Specification for Seismic Energy Dissipation of Buildings, Ministry of Housing and Urban-Rural Development of the People's Republic of China, Beijing, China, 2013 (in Chinese).

[24] R.W. Clough, Dynamics of Structures, Computers & Structures, Inc. University Ave Berkeley (CA 94704, USA), 1995.

[25] ABAQUS version 6.14: ABAQUS User's Manual, SIMULIA World Headquarters. Rissing Sun Mills 166 Valley Street, Providence(RI 02909–2499, USA), 2014.

[26] Z. Mroz, H.P. Shrivastava, R.N. Dubey, A non-linear hardening model and its application to cyclic loading, Acta Mech. 25 (1–2) (1976) 51–61, https://doi.org/10.1007/bf01176929.

[27] C. Chou, Y. Sheng, Subassemblage tests and finite element analyses of sandwiched buckling-restrained braces, Eng. Struct. 32 (8) (2010) 2108–2121, https://doi.org/10.1016/j.engstruct.2010.03.014.

[28] N. Hoveidae, B. Rafezya, Overall buckling behavior of all-steel buckling restrained braces, J. Constr. Steel Res. 79 (12) (2012) 151–158, https://doi.org/10.1016/j.jcsr.2012.07.022.